Generating High Power Terahertz and Far Infrared Electromagnetic Radiation with Relativistic Electrons

N. A. Vinokurov[1, 2]

[1]Budker Institute of Nuclear Physics SB RAS, Novosibirsk, Russia, vinokurov@inp.nsk.su
[2]Novosibirsk State University, Novosibirsk, Russia

Relativistic electron beams are used successfully to generate electromagnetic waves. Both narrow-band and short-pulse THz generators of such type are described with examples of the free electron lasers (FELs) and prebunched-beam devices.

FELs (see, e.g., [1]) convert the power of relativistic electron beams to narrow-band radiation. The main component of an FEL is a special spatially periodic magnetic system, called undulator (see, e.g., [2]). The undulator magnetic field curves electron trajectories; therefore, electrons emit narrow-band electromagnetic radiation in free space. The scheme of the FEL amplifier is shown in Fig. 1.

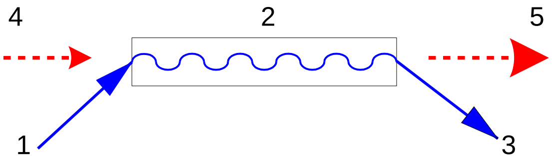

Fig. 1. The scheme of FEL amplifier: 1 – incoming electron beam, 2 – undulator, 3 – used electron beam, 4 – incoming electromagnetic wave, 5 – amplified electromagnetic wave

FELs use a phenomenon of the stimulated undulator radiation. i. e. bunching of electrons by an external electromagnetic wave and an increase of the wave field amplitude by addition of the field emitted by the bunched electron beam. On the other hand, FEL can be considered as travelling wave tube. Then undulator is necessary to provide (i) interaction of electrons with transverse electromagnetic wave and (ii) fast space harmonic of transverse electron current.

The particular problem of terahertz FELs is large diffraction divergence of the amplified wave. It require either large aperture of undulator, or the use of waveguide inside undulator. The first solution leads to the increase of the undulator period and corresponding increase of the electron energy. Moreover, big diameter of radiation beam leads to lower amplitude of electromagnetic field (at fixed power) and lower amplification. The second option is suffers from significant power losses. Therefore, it requires high enough FEL gain. For high average power FEL, the sufficient waveguide cooling has to be provided.

Another issue of FELs is the way to vary the radiation wavelength. The wavelength of the undulator radiation

$$\lambda = \frac{\lambda_u}{2\gamma^2}\left(1+\frac{K^2}{2}\right) \qquad (1)$$

depends on the undulator period λ_u, the electron energy γmc^2 and the undulator parameter $K = eB\lambda_u/(2\pi mc^2)$ (c is the velocity of light, e and m are the charge and the mass of electron, correspondingly), which is proportional to the amplitude B of magnetic field. The most straightforward way is to vary the electron energy. However, in fact, it is rather complicated, as require changing many parameters of an electron accelerator, which is typically optimized for some particular energy. The variation of the magnetic field amplitude is the most common now. It is achieved by variation of current in the coils of electromagnetic undulators or by variation of the gap between upper and lower parts of permanent magnet undulators. The drawback of the field amplitude variation is that at shortest wavelength of the tunability range the undulator performance is far from the optimal one. Indeed, for such a low field amplitude, one can build an undulator with shorter period and larger pole numbers at the same length. Last decade we developed the third option – the variation of the undulator period [3, 4]. Variable period permanent magnet undulators were built and tested successfully [5, 6]. Next year we plan to install the variable period undulator to Novosibirsk FEL facility (see [7, 8]). It will replace one of the old electromagnetic undulators there.

For some applications, short high-field pulses are required. Contemporary accelerator technology provides very short electron bunches. The common way to do it is the use of radiofrequency (RF) electron guns with photocathodes (see, e.g., [9]). Using commercial lasers one can obtain few-picosecond electron bunches with electric charge Q of about 1 nC and normalized emittance of about 1 micron. The bunch charge is limited by Coulomb repulsion of electrons inside the RF gun. After acceleration, the bunch can be compressed to sub-picosecond duration T. Then the energy of the field around the bunch, which can be converted to the electromagnetic pulse energy, $W \sim Q^2/(cT)$ may reach 1 mJ. One of the possible radiators in this case is transition radiation, when the bunch passes through a conducting foil. The efficiency of such radiator may be enhanced using many foils and combining signals from them. The example of such a device, the multifoil radiator [10], is shown in Fig. 2. Short electron bunch passes through the conical foil stack along the cone axis z. After the bunch has passed through the gap between two of the foil disks, the induced electromagnetic wave propagates radially outward. As the pulses reach the foil boundaries, they merge and form the conical radially polarized wave. One can also say that this radiator is the Cherenkov one with strongly anisotropic media. The device was tested [11] with the short bunch from laser plasma wakefield accelerator.

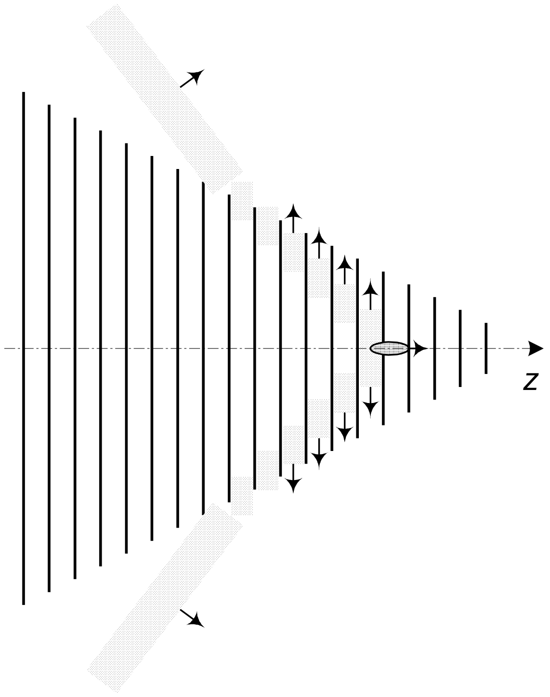

Fig. 2. The scheme of the conical multifoil radiator

Acknowledgment

This work was supported by the Russian Science Foundation (project No. 14-50-00080).

References

1. *Vinokurov, N. A., Shevchenko, O. A.* Free electron lasers and their development at Budker Institute of Nuclear Physics SB RAS // Phys. Usp. 2018. V. 61, No. 5. P. 435–448.

2. *Vinokurov, N. A., Levichev, E. B.* Undulators and wigglers for the production of radiation and other applications // Phys. Usp. 2015. V. 58, No. 9. P. 850–871.

3. *Shenoy, G. K., Lewellen, J.W., Shu, D., Vinokurov, N.A.* Variable-period undulators as synchrotron radiation sources // J. Synchrotron Radiat. 2003. V. 10. P. 205–213.

4. *Vinokurov, N. A., Shevchenko, O. A., Tcheskidov, V. G.* Variable-period permanent magnet undulators // Phys. Rev. Spec. Top. - Accel. Beams. 2011. V. 14, P. 040701–1 - 040701–7.

5. *J. Mun, et al.* Variable-period permanent-magnet helical undulator // Phys. Rev. Spec. Top. - Accel. Beams. 2014. V. 17, P. 080701–1 - 080701–6.

6. *Davidyuk, I.V., Shevchenko, O. A., Tcheskidov, V. G., Vinokurov, N. A.* Results of test of prototype of variable period undulator // Nucl. Instr. & Meth. A. 2017. V. 871, P. 77–82.

7. *Shevchenko, O. A. et al.* The Novosibirsk Free Electron Laser – unique source of terahertz and infrared coherent radiation // Phys. Procedia 2016. V. 84. P. 13–18.

8. *Knyazev, B. A. et al.* Novosibirsk free electron laser as a user facility // Phys. Procedia 2016. V. 84. P. 27–34.

9. *Vinokurov, N. A. et al.* Electron guns at the Budker Institute of Nuclear Physics SB RAS: prospects for the use of photocathodes with nanosecond and subpicosecond laser drivers // Phys. Usp. 2017. V. 60, No. 10. P. 1034–1038.

10. *Vinokurov, N. A., Jeong, Y. U.* Generating High-Power Short Terahertz Electromagnetic Pulses with a Multifoil Radiator // Phys. Rev. Lett. 2013. V. 110, No. 6. P. 064805-1 – 064805-5.

11. *Jo, J. et al.* High-power ultrashort terahertz pulses generated by a multifoil radiator with laser-accelerated electron pulses // Proc. of FEL2015, Daejeon, Korea. 2015. P. 739-740. http://accelconf.web.cern.ch/AccelConf/FEL2015/papers/wep082.pdf .

Terahertz Probing of Topological Surface Electron States

Dmitry Khokhlov[1,2], A. V. Galeeva[1], L. I. Ryabova[3]

[1]Physics Department, M.V. Lomonosov Moscow State University, Moscow, Russia, khokhlov@mig.phys.msu.ru
[2]P.N. Lebedev Physical Institute, Moscow, Russia
[3]Chemistry Department, M.V. Lomonosov Moscow State University, Moscow, Russia

Three-dimensional topological insulators (TI) belong to a fascinating class of quantum matter and display fundamentally different electron energy spectrum at the surface and in the bulk. The bulk energy spectrum of a TI is typical for a semiconductor, whereas spin-polarized gapless electron states with the linear dispersion relation exist on the TI surface. Theoretical prediction of topological surface electron states and their further observation by angle resolved photoemission spectroscopy for narrow-gap Bi_2Se_3 semiconductors initiated extensive studies of electron transport aimed at revealing the topological electron states. On the other hand, ARPES does not provide direct information on the surface conductivity, and the main interest to topological surface states was stimulated by hopes to use the electron transport via these states. This electron transport is topologically protected against backscattering, and the carrier effective masses are very small due to the Dirac energy spectrum of the TI states. In most of the cases, however, this surface electron transport is shunted by conductivity via the bulk of a sample since most of the topological insulators are narrow-gap semiconductors with the Fermi level lying on the background of either conduction or valence band. The second approach that is applied in this paper uses optical excitation of surface electron states. It turns out that this approach is not very sensitive to the bulk conductivity and provides therefore valuable information on features of conducting surface states.

The second methodological aspect used in our experimental approach is the following. Comparison of experimental data corresponding to the topological and trivial phases is expected to be very helpful in extraction of transport features of TI. Therefore materials that manifest a transition from the topological to the trivial phase are of a special interest. Mixed $(Bi_{1-x}In_x)_2Se_3$ crystals are a brilliant example of such materials, for which this kind of transitions has been observed in the range of compositions $x \approx 0.03 - 0.07$ according to different dataset available.

$(Bi_{1-x}In_x)_2Se_3$ $(0 \le x \le 0.18)$ single crystals were grown by the Bridgman method. The alloy composition x was determined by the XRD and X-ray fluorescence analysis. Photoluminescence spectra of the samples were taken to define the energy spectrum parameters. The PL spectra show that the bandgap decreases with increasing temperature for samples with the inverse energy spectrum, and it rises for direct spectrum samples. It has been determined that in the range of $(Bi_{1-x}In_x)_2Se_3$ solid solutions, the bandgap varies with the rate of $dE_g/dx = 41$ meV/mol.%, and the gapless state corresponds to $x \sim 0.06$.

The Hall effect measurements reveal that all samples are highly degenerate semiconductors with the free electron concentration ~ 10^{19} cm^{-3} and mobility varying in the range ~ $10^2 - 10^3$ $cm^2V^{-1}s^{-1}$. We have studied the photoelectromagnetic (PEM) effect under the action of terahertz laser radiation. This effect manifests itself as a voltage drop across the sample in the direction perpendicular to the magnetic field applied in-plane of a sample, and the incident radiation is normal to the sample surface. The PEM effect was studied at temperatures 4.2 K – 20 K in magnetic fields up to 3 T using laser pulses at the wavelengths of 90, 148 and 280 μm. The peak power of the incident radiation was up to 10 kW and varied by calibrated attenuators.

The PEM effect was observed in all the samples at $T < 14$ K, at all laser wavelengths employed. The PEM effect signal repeats the temporal shape of a laser pulse. In all samples studied, the peak PEM effect voltage (the PEM effect amplitude, U_{PEM}) linearly depends on the magnetic field in low fields $B < \sim 1.5$ T, after which the U_{PEM} value saturates. The PEM effect sign corresponds to the net electron flux directed from the sample surface to its bulk. Since the energy of the terahertz radiation quanta is about 10 meV which is much less than the Fermi energy in the samples studied (~ 130 meV), photogeneration of extra free charge carriers is impossible. The net electron flux from the sample surface results from a gradient in electron mobility between the sample surface and its bulk and is an evidence of enhanced mobility values of the surface electrons both in the topological and trivial phases. The close PEM amplitude meanings observed for samples with different bulk mobility magnitudes demonstrate that PEM effect turns out to be insensitive not only to the bulk carrier concentration but to the bulk mobility as well.

The samples with $x = 0$ and $x = 0.12$ which are characterized by close energy gaps and free electron concentrations, but possess either inverse, or direct energy spectrum were chosen for the detailed study of the PEM effect. U_{PEM} depends almost linearly on P for a given value of λ both for $x = 0$ and $x = 0.12$. At the same time, in the sample with $x = 0.12$ being in the trivial phase, the PEM effect amplitude practically does not depend on the wavelength of the incident radiation, whereas it does depend on λ for the sample with $x = 0$ being in TI phase. On the contrary, the U_{PEM} value calculated as a function of the number of incident radiation quanta $N = P\lambda/hc$ does not depend on the laser wavelength for the sample with $x = 0$ and does depend on it for sample with $x = 0.12$.

Such a behavior may arise from fundamentally different relaxation processes features for non-equilibrium carriers in TI and TS. If the excited electrons first thermalize in the surface area and afterwards the diffusion process begins, giving rise to the PEM effect signal, the net diffusive electron flux is defined by the electron temperature gradient between the surface layer and the bulk which is governed by the radiation power absorbed. In case of electron gas thermalization time enhanced the diffusion of unthermalized electrons from the surface turns out to be a limiting process which leads to the PEM effect defined by the incident photon density. It can be supposed that in TI thermalization time of the non-equilibrium carriers may be enhanced due to strong damping of interaction between spin-polarized electrons in the topological layer.

Another example of a system that undergoes a transition from the topological phase to the trivial one upon change in the composition are mercury cadmium telluride $Hg_{1-x}Cd_xTe$ solid solutions. At $x < \sim 0.16$ these semiconductors demonstrate an inverted band structure ordering which corresponds to the topological phase. The conduction band and the heavy hole subband touch each other providing a gapless state in the whole composition range $0 < x < 0.16$. The positive energy gap opens, and the trivial state is realized at $x > 0.16$. In contrast to the most of 3D topological phases, the free carrier concentration in $Hg_{1-x}Cd_xTe$ topological phase is low enough to observe the photoconductivity effect in the terahertz spectral range.

In this work, we present our experimental results on the photoconductivity excited by terahertz laser pulses in $Hg_{1-x}Cd_xTe$ epitaxial films in a close vicinity to the band inversion point. We demonstrate that, for the topological phase, the photoresponse is an uneven function of the magnetic field applied. This behavior is atypical for the conductivity and photoconductivity which normally do not depend on the magnetic field polarity.

$Hg_{1-x}Cd_xTe$ films of ~ 5 μm thickness were deposited on a semi-insulating GaAs (013) substrate with ZnTe and CdTe buffer layers by the molecular beam epitaxy. The free electron concentration determined from Hall measurements is $\sim 3 \cdot 10^{14}$ cm^{-3} at T = 4.2 K. The photoconductivity measurements were performed for the Hall bar samples with $x < 0.16$ (topological phase, inverted band structure), and $x > 0.16$ (trivial phase, normal band structure) in the Faraday geometry at T = 4.2 K. The photoexcitation was carried out using pulsed laser radiation with a wavelength varying from 90 to 496 μm. Duration of laser pulses was about 100 ns. Magnetic field applied was up to 4 T.

We have observed the positive and the negative photoconductivity effects in the absence of the magnetic field in the samples with the inverted and the direct energy spectrum, respectively. The negative photoresponse is related to the electron gas heating, while the positive photoconductivity is due to the interband transitions.

It has been found that the photoresponse in the samples being in the topological phase strongly depends on the combination of both the magnetic field polarity and the potential probe position. For a given pair of the potential probes, the photoconductivity in weak magnetic fields B < 1 T is featured by the positive contribution which is absolutely suppressed for the opposite magnetic field direction, as well as for the mirror-like potential probes across the sample. The negative photoconductivity prevails in strong magnetic fields B > ~1 T. The asymmetric photoresponse in magnetic field may be due to the spin-related features of the carriers in topological phase.

The photoresponse practically does not depend on the magnetic field and is insensitive to the magnetic field polarity and the probe position for samples being in the trivial phase.

Normally, the conductivity and photoconductivity do not depend on the magnetic field polarity. We suggest that the effect is due to the diffusion of photoexcited electrons from the bulk to the topological layer at the interface between the trivial buffer and the topological film. Linking of the spin direction to the momentum direction plays a crucial role in the mechanism of the effect appearance that is suggested.

Investigations of hydration dynamics in biomedical systems using terahertz waves

Kihoon Eom[1], Jungmin Jang, Inkyung Park, Sunmyeong Kim, Seungmok Yum, Juhan Kim, Kyunghoon Jung, Haesung Lee, Debashis Majhi, and Gun-Sik Park[1]

[1]Department of Physics and Astronomy, Seoul National University, Seoul, Korea, gunsik@snu.ac.kr

Water is essential for most life processes and the most biological and chemical processes occur in an aqueous environment. It is believed that water strongly influence the structure and function of biomolecules as an active partner. Water molecules in liquid state has a very complex structure which is connected by hydrogen bonds with surrounding molecules. Typically, liquid water forms four hydrogen bonds which form tetrahedral structure of water molecules. This water structure constantly fluctuates via breaking and forming of hydrogen bonds. Therefore, the structure and dynamical properties of liquid water have long been a subject of many researchers in the environment of various biomedical systems such as biomolecules, ion solution and skin. Various experimental and theoretical study were used to understand detailed structure and dynamic properties of water molecule. In this presentation, the hydration dynamics investigated in the biomedical systems including membrane hydration, ion hydration and skin hydration using terahertz waves will be presented.

The properties of interlamellar water are critically important to the structure and function of biological membranes. The most relevant interactions include weak hydrogen bonds among water molecules and between water and the polar or ionic groups of the biomolecule, long-range Coulomb forces, and hydrophobic forces. Various experimental techniques have been used to study the properties of hydrating membranes, including neutron scattering [1,2], nuclear magnetic resonance (NMR) spectroscopy [3,4], infrared spectroscopy [5], ultrafast vibrational spectroscopy [6], and terahertz spectroscopy [7]. Dielectric spectroscopy used in this study is an important tool to obtain information of intermolecular dynamics of water molecules in fluctuating hydrogen bond network. Debye describes the dielectric constant of water in GHz region in terms of dielectric relaxation due to the diffusive rotational motion of water molecule. Recently, dielectric response in THz region has not been described as a single mode of Debye relaxation but as with another relaxation mode in the THz domain with faster timescale. Especially the nanoconfined water inside MLV draws a great attention as a platform to investigate the various aspects of the hydration dynamics in such an extreme situation where specific interface and confinement need to be taken into a consideration. Nanoscopically encapsulated environment can be seen in various biological complexes. The concerns in this study is to understand the hydration dynamics in this nanoscopically confined environment. Broadband GHz-THz dielectric relaxation spectroscopy is employed to observe the various modes inside MLV. The dynamic light scattering and X-ray technique are used to estimate the size and inter-lamillar spacing in MLV. The hydration dynamics influenced by the interface and nanoscopically confined situation is discriminated using the broadband dielectric relaxation spectroscopy. This work can be a basis for nanofluidics and water transport in nanostructures. However, molecular level understanding is still unclear. The molecular dynamics simulation work is underway.

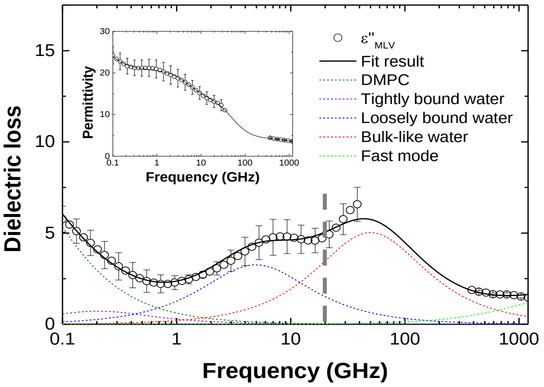

Effect of ion on water structure is conceived as ion-specific, classified as structure making ion and structure breaking ion. Macroscopic properties of water such as viscosity is related with effect of ion on water structure. Generally, multiply charged small ion has strong ability to water structure making and monovalent large ion behave as structure breakers. These ion-specific trends can also be found in Hofmeister series which is related with effect of ion on aggregation of proteins. Also ion affects dynamic properties of water in aqueous solution. Previous spectroscopic experiment results[8] show that ion makes waters which is slowly reorienting compare to the pure water. THz-dielectric relaxation spectroscopy and IR spectroscopy observed “slow-water” molecule increases for various salt solution. In this experiment, combined THz-dielectric spectroscopy and fs IR spectroscopy have shown effect of ion on water dynamics is well beyond first hydration shell and caused by cooperative interaction with cation and the anion. From the viewpoint of fast relaxation mode, THz dielectric relxation spectroscopy found that fast relaxation mode changes in different salt solutions. In these studies, fast relaxation mode is connected previously suggested model that fast water mode comes from fast reorienting water molecule which have no H-bond with surrounding water molecules. it is shown that dissolved ion weakens the hydrogen bonding network of water in ionic solution and this results in fast relaxation increases in various salt solution. The fast relaxation mode change was ion specific. In the case of structure breaking ion, the fast relaxation mode was larger than that of the other ions. In case of strong structure making ion, the fast relaxation mode tended to decrease rather than pure water. In spite of recent experimental results, there is still lack of molecular level understanding how the fast water mode changes by adding ion in aqueous solution.[9] Therefore, main goal of this study is to explain how and where the fast reorienting water formed in salt solution and confirm the previously suggested models for fast water mode (water molecules with one H-bond or water molecules with no H-bond) by connecting dielectric relaxation spectroscopy and MD simulation of salt solution. In the MD simulation, we categorize different water molecule kind by using distance criteria between cation and water oxygen (anion and water hydrogen). Previous studies propose effect of ion on reorientation dynamics of water molecule as cation interact with water molecule and affect the reorientation dynamics of water dipole moment and anion affect the reorientation dynamics of OH arms of water. Therefore, we can separate water molecules which is locked both axis (dipole/OH arms) by cation and anion and water molecules surrounding this "locked" domains using above classification. We show that water molecules in locked domains show slow reorientation dynamics compare to the pure water as suggested in previous study and water molecules surrounding this locked domain has less H-bond structure because structure breaking effect due to ion, thus showing fast reorientation motion compare to the pure water. Also we present evidence of this "surrounding domain" water really contributes to fast relaxation mode by comparing fraction of water molecule showing fast relaxation mode from experiment and fraction of "surrounding domain" in the simulation. This two fraction shows highly correlated dependence on salt concentration in different kind of aqueous solution of MgCl2 and CsCl (Strong structure maker/breaker).

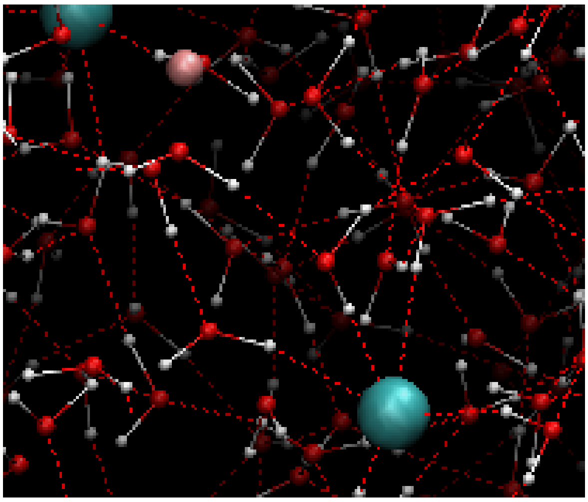

The hydration dynamics in human skin is studied to understand the friction mechanism. we assayed the coefficient of kinetic friction in case of 'normal' and 'wet' fingertips. Normal load of each test was monitored to maintained around 1.0 N same as measurement of the hydration level. Interestingly, coefficient of kinetic friction shows highest value at steady-state of hydration value. These results suggest that the hydration level of fingertip converges to an important value of C_∞ that maximizes grip friction. Various experimental techniques are employed to elucidate the mechanism. [10]

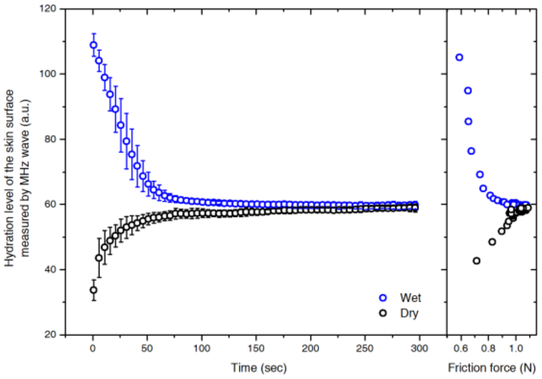

References

1. Fitter, J.; Lechner, R.E.; Dencher, N.A., J. Phys. Chem. B 1999, 103, 8036–8050.
2. Trapp, M.; Gutberlet, T.; Juranyi, F.; Unruh, T.; Demé, B.; Tehei, M.; Peters, J. , J. Chem. Phys. 2010, 133, 164505.
3. Mazza, M.G.; Stokely, K.; Pagnotta, S.E.; Bruni, F.; Stanley, H.E.; Franzese, G. , Proc. Natl. Acad. Sci. USA 2011, 108, 19873–19878.
4. Wassall, S.R. , Biophys. J. 1996, 71, 2724–2732..
5. Volkov,V.V.;Palmer,D.J.;Righini,R. , Phys. Rev. Lett. 2007, 99, 078302.
6. Zhao, W.; Moilanen, D.E.; Fenn, E.E.; Fayer, M.D. , J. Am. Chem. Soc. 2008, 130, 13927–13937
7. Tielrooij, K.J.; Paparo, D.; Piatkowski, L.; Bakker, H.J.; Bonn, M. , Biophys. J. 2009, 97, 2848–2492.
8. K. J. Tielrooij, N. Garcia-Araez, M. Bonn, H. J. Bakker, Science, 2010, 328, 5981
9. Alex P. Gaiduk and Giulia Galli, J Phys. Chem. Lett., 2017, 8(7)
10. The result is submitted for the publication.

Femtosecond Acoustics and Terahertz Ultrasonics

Chi-Kuang Sun

Graduate Institute of Photonics and Optoelectronics, National Taiwan University, Taipei, Taiwan, sun@ntu.edu.tw

Acoustic wave is one of the most natural tools for communication and imaging. It is used for clinical imaging, to noninvasively probe physical structures under the surface as well as thermal dynamics of objects. However, considering the bandwidth (GHz) of current ultrasonic technologies, the electrically generated acoustic wave has a pulse duration much longer than 1 ns and a wavelength longer than 10 μm, which is far from adequate for molecular-level imaging, not to mention the femtosecond dynamics of many interacted molecules, including liquid water. Besides, it is believed that a wave-particle transition of THz acoustic waves must come into play when they are interacting with thermal phonons in all kinds of materials, including thin films, bulk materials, and nanostructures. To resolve the mysterious thermal dynamics in amorphous materials as well as the energy (heat) transport and dissipation from solids into liquids, an ultra-broadband THz acoustic source is thus urgently needed.

In this presentation, I would like to present the result of a new research direction: femtosecond acoustics and terahertz ultrasonics. The physical principle to convert a femtosecond optical pulse into a femtosecond acoustic pulse will be introduced. With a short pulse width, the spectral bandwidth can thus exceed THz. Combined with the ultraslow sound velocity, the application of this new tool is two folds. One is for THz phonon spectroscopy, which is critical to resolve the heat transport mysteries. The other is for in situ noninvasive sub-surface atomic level resolution imaging, which was not possible before. Examples will be given in this presentation.

Since it's proposed by H. Maris 30 years ago, "picosecond ultrasonic" has been developed as a complete technique able to study various acoustic phenomena and parameters from thickness measurements [1] to hypersound attenuation [2,3]. Based on the use of an ultrafast laser, this technique allows the generation and detection of coherent acoustic phonons (CAP) in the sub-THz range. Even though picosecond ultrasonic has been developed for more than 30 years, its frequency range can only reach 400GHz, which is still far from THz. In 1999, by femtosecond laser excitation of piezoelectric semiconductor quantum wells, we discovered a simple way to generate giant coherent acoustic phonons (acoustic waves) with a frequency over 2 THz [4]. This piezoelectric nano-layer based technique was later-on termed "nano-ultrasonics," with a focus to emphasize its capability to provide nano-meter spatial resolution ultrasonic images [5]. After over one decade's study, we have made this technique a powerful tool to image and characterize nanoscale materials and interfaces. In recent years, this method has not only been successfully applied to characterize the ångström-level surface and interface roughness [6], but also the acoustic attenuation up to 650 GHz in amorphous SiO_2 and more recently we showed the possibility to measure the acoustic attenuation spectrum in ice up to 1 THz, thus providing critical thermal dynamics parameters [7].

During my presentation, I will show the effort of the current program to not only continuously apply the THz acoustic spectroscopy 1). for the investigation of the Boson peak issue in amorphous solids and 2). of the collisionless decay of the coherent phonons in crystals, but also 3). to work on the atomic resolution imaging in solid-liquid water interface.

Amorphous material systems have impacted human lives in numerous aspects. Glasses, polymers, and even bio-tissues are significant matters made with amorphous structures. Despite the long appearance, the physical natures of the amorphous material system are still far from well understood. Unlike crystalline solids, amorphous materials exhibit a number of anomalous thermal properties. These anomalies were first discovered half a century ago by Berman, who noticed the unexpected instance of the thermal conductivity $\kappa(T)$ anomaly for vitreous silica (v-SiO_2). He measured the thermal conductivities of several v-SiO_2 samples in the temperature range between 2.2 and 90K and found the plateau behavior of thermal conductivities at around 10K, corresponding to a phonon peak frequency of ~1THz, with a magnitude several orders smaller. Since then, several other techniques, such as Raman scattering, inelastic neutron scattering, and X-ray scattering, had been carried out to explore this anomalous thermal phenomenon. Although many had witnessed the anomaly, none of them were able to provide a comprehensive understanding of its origin.

In crystals, the low-frequency density of states (DOS), $g(\omega)$, follows the so-called Debye model well; that is, by simply considering possible modes of sound waves which match the boundary conditions, one obtains the square frequency dependence of the DOS, $g(\omega)\propto\omega^2$. In contrast, amorphous material systems show an excess contribution to the DOS at the THz frequency regime (or at ~5meV energy level appeared in inelastic scattering spectra), which in turn results in a decreased thermal conductivity or an increased specific heat, as evidenced by previous vitreous silica experimental results. The excess in DOS is usually identified as a peak in a reduced DOS representation, $g(\omega)/\omega^2$ vs ω. At the time of its discovery, little was known about this feature except for its bosonic character. Therefore, it became known as the "boson peak" (BP). The physical origin as well as dynamics of the Boson Peak remained puzzling and controversial due to the fact that no acoustic attenuation spectral measurement in this frequency range can be directly performed in amorphous materials to verify the correctness of different theoretical models.

In contrast to amorphous solids, in past decades, hypersound wave propagation in crystalline solids have drawn much attention in a wide variety of scientific studies focusing on topics such as the spontaneous decay of longitudinal acoustic phonons, picosecond ultrasonics, nanoultrasonics, and the development of acoustic phonon lasers. In the frequency range of 0.4-3THz, coherent acoustic phonons (or hypersound waves) in crystal are physically modeled to be attenuated due to collisions with thermal phonons. However, different theories were debated with no experimental proof to distinguish their correctness and appropriate frequency ranges.

In crystalline dielectrics, this hypersound propagation loss can arise from both extrinsic and intrinsic mechanisms. The extrinsic mechanisms are commonly dominated by phonon-scattering processes at lattice imperfections. When these extrinsic mechanisms are absent, the acoustic loss will ultimately be determined by intrinsic anharmonic decay. Based on low frequency data, the mostly accepted picture is as follow. In most solids, thermal phonons have a lifetime, τ, on the order of picosecond to femtosecond. When the angular frequency, ω, of the acoustic waves is small compared to the thermal phonon lifetime with $\omega\tau$<<1 (usually in the sub-THz range), the propagation of acoustic waves will drive the thermal phonons out of equilibrium, and causing the interaction and resulting in the acoustic wave attenuation. Due to the fact that the acoustic waves are with a wavelength much longer than most room-temperature thermal phonons, the propagating coherent phonons will be scattered by all different thermal phonons and the momentum conservation is not a concern, due to the large uncertainty. This model well describes all lower-frequency (below 400GHz) measurement on different solids.

However it has been long debated and postulated that, when $\omega\tau$>>1 (usually above THz at room temperature), acoustic waves have to be considered as coherent phonons and the attenuation of coherent phonons due to their interaction with thermal phonons will be limited due to specific selection rules for energy and momentum conservation. That is to say that, only selected thermal phonons with specific momentums and energies involve in this “3-phonon interaction” process, thus making THz acoustic wave attenuation “saturated.” In the transition range between these two regimes, $\omega\tau$>>1, the acoustic frequency will be around THz for room temperature crystals.

In this frequency range, the coherent acoustic phonon attenuation processes have never been explored and have been under debate for almost four decades due to the lack of reliable THz acoustic transducers. Applying our developed THz nano-ultrasound technique and studying the frequency dependent behavior of coherent acoustic phonons in this ambiguous transition range is therefore crucial since it will bring critical understanding for thermal properties in solids.

For nanoimaging with a femtosecond acoustic pulse, one can take advantage of the ultraslow sound velocity, which is usually on the order of 3000 m/s and the ultrahigh temporal resolution which is usually on the order of 100 fs. It can be noted that within 100 fs, a femtosecond acoustic pulse travels only a distance of 3 angstroms, assuming a 3000 m/s velocity. Femtosecond time-resolved sound propagation imaging can thus provide a spatial resolution down to 1.5 angstroms assuming an acoustic round trip path. To study the performance of femtosecond acoustics applied on *in situ* monitoring a chemical reaction at a solid/liquid interface, the well-known anode-oxidation process occurring during the GaN-based photo-electro-chemical (PEC) water splitting was taken as our model. As a result, sub-atomic resolution imaging was observed in situ noninvasively [8].

This project is sponsored by Ministry of Science and Technology of Taiwan under 106-2112-M-002 -004 -MY3 and National Taiwan University under 107L880404.

References

1. *Thomsen, C., Grahn, H. T., Maris H. J., Tauc, J.* Surface generation and detection of phonons by picosecond light pulses // Phys. Rev. B, 1986. V. 34, No. 6, P. 4129-4138.

2. *Lin, H. N., Stoner, R. J., Maris, H. J., Tauc, J.* Phonon attenuation and velocity measurements in transparent materials by picosecond acoustic interferometry // J. Appl. Phys., 1991. V. 69, No. 7. P. 3816-3822.

3. *Duquesne, J.-Y., Perrin, B.* Ultrasonic attenuation in a quasicrystal studied by picosecond acoustics as a function of temperature and frequency // *Phys. Rev. B*, 2003. V. 68, No. 13. 134205.

4. *Sun, C. K., Liang, J. C., Yu, X Y.* Coherent acoustic phonon oscillations in semiconductor multiple-quantum-wells with piezoelectric fields // *Physical Review Letters* 2000. V. 84, No. 1, P. 179-182.

5. *Lin, K.-H., Lai, C.-M., Pan, C.-C., Chyi, J.-I., Shi, J.-W., Sun, S.-Z., Chang, C.-F., Sun, C.-K.* Spatial manipulation of nanoacoustic waves with a nanoscale spot size // Nature Nanotechnology 2007. V. **2,** No. 11, P. 704-708.

6. *Wen, Y.-C., Hsieh, C.-L., Lin, K.-H., Chen, H.-P., Chin, S.-C., Hsiao, C.-L., Lin, Y.-T., Chang, C.-S., Chang, Y.-C., Tu, L.-W., Sun, C.-K.* Specular scattering probability of acoustic phonons in atomically flat interfaces // Physical Review Letters 2009. V. 103, No**.** 26. 264301.

7. *Mante, P.-A., Chen, C.-C., Wen, Y.-C., Sheu, J.-K., Sun, C.-K.* Thermal boundary resistance between GaN and cubic ice and THz acoustic attenuation of cubic ice from complex acoustic impedance measurements // Physical Review Letters 2013. V. 111, No. 22. 225901.

8. *Shen, C.-C., Weng, M.-Y., Sheu, J.-K., Yao, Y.-T., Sun, C.-K.* In situ monitoring of chemical reactions at a solid-water interface by femtosecond acoustics // Journal of Physical Chemistry Letters 2017. V. 8, No. 21. P. 5430-5437.

Biomedical applications of microwave radiation: innovative approaches

Andrew Martusevich[1,3], A. V. Kostrov[2]

[1]Privolzhsky Research Medical University, Nizhny Novgorod, Russia, cryst-mart@yandex.ru
[2]Institute of Applied Physics, Nizhny Novgorod, Russia
[3]Kirov State Medical University, Kirov, Russia

Now it is widely known postulate that all the major discoveries in recent years occur at the junction of different sciences. In this regard, one of the most important innovative areas uniting physics, biology and medicine is the use of microwave technologies. In this regard, the purpose of this work was to clarify the practical possibilities of diagnostic and therapeutic microwave technologies.

Microwave technology in medical imaging

Medical visualization is currently one of the most dynamically developing areas of medical science. Analysis of the literature on the methodology of microwave imaging, implemented in Biomedicine, allows us to identify two main sensing techniques that differ in the estimated parameters: microwave thermometry (passive) and near-field resonance tomography.

In the framework of microwave thermometry (radiometry), the volume dynamics of the subsurface temperature distribution is recorded by the trapping device. At the same time, it is known that in a number of pathological conditions (for example, in oncomammology) there is a significant local hyperthermia, which will be detected by a microwave sensor.

On the contrary, in recent decades actively developed by resonant near-field microwave imaging, allowing you to visualize the structure of biological tissues on the basis of spatial distribution their electrodynamic characteristics - dielectric constant (ε) and conductivity (σ) [Fig. 1], characterizing the type and structural features of the biological object. The possibility of using this type of tomography for diagnostic purposes is due to the fact that the formation of pathological changes in biological tissues is a distinct change in their electrodynamic characteristics.

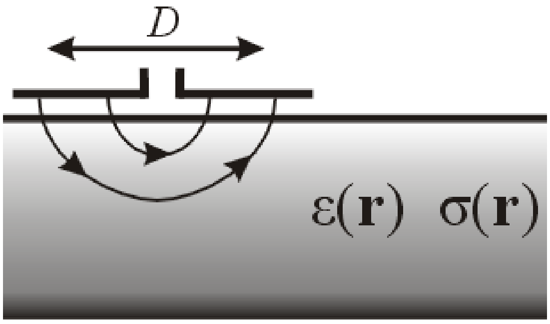

Fig. 1. Scheme of the stud of dieectric characteristics of the object

Near-field resonance microwave diagnostics is based on the measurement of electrodynamic characteristics of biological tissues. Work in this direction with biomedical positions are relatively recent, but the physical principles underlying near-field microwave tomography, studied much more fully. Thus, the fundamental basis of the method is the measurement of impedances located on the surface of the bio-object of a system of electrically small antennas with different scales of localization of the probing electric field. The spatial distribution of dielectric permittivity and electrical conductivity of tissues is restored by the values of impedances (active and reactive resistance) of antennas on the basis of a special mathematical apparatus.

Measuring the impedance of antennas is implemented in a special resonant sensor. The sensor is a microwave resonator in the form of a transmission line segment (coaxial, two-wire or strip) [1]. At one end of this segment there is a probing near-field antenna (measuring capacitance), at the opposite end there is a magnetic frame. Excitation of the resonator and reception of its response is carried out by means of magnetic coupling loops located near the magnetic frame of the resonator. All elements of the resonance system, except for the measuring capacitance, are located in a metal cylindrical body. Own resonant frequency of the sensor, as a rule, is in the range of 600-800 MHz, the characteristic quality factor – 150.

The scheme illustrating deep sounding of biological tissue within the near-field microwave tomography is presented in Fig. 2. Near-field antenna is located on the surface of the object under study, its quasi-static electric field penetrates into the medium to a depth determined by the design of the antenna and the size of its aperture (D). The depth of penetration of the electric field into the medium will increase with increasing aperture D.

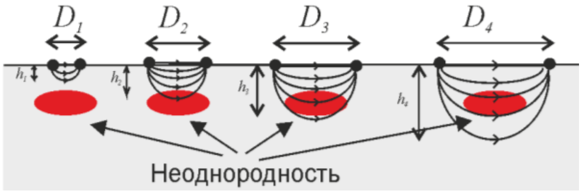

Fig. 2. Scheme of a deep sensing of inhomogeneous media by the method of resonance near-field microwave tomography

The study of heterogeneous biological media is carried out as follows. First, the measurements are carried out by the sensor with the lowest D_1 value and, accordingly, with the lowest sounding depth h_1, the measurement results reflect the integral properties of the medium in the surface layer. For sensor with sensing h_2 depth □ integral properties of the medium in the near-surface layer of greater thickness, etc. Knowing the responses of measuring systems with different sensing depths, it is possible to restore the deep structure of the inhomogeneous medium.

Have presently developed near-field diagnostic systems key value "the size of the aperture of the probe (D) / wavelength of the probing microwave signal (λ)" comes to the level of 10^{-5}-10^{-6} that in comparison with the wave techniques gives the opportunity to examine the condition and structural features of the tissue on their electro-dynamic properties with subwavelength spatial resolution (much smaller than the wavelength λ).

Thus, near-field resonance microwave sensing, thanks to its physical principles, makes it possible to vary the depth and surface area of the study of biological objects, using electrodynamic characteristics of the medium - its dielectric permeability and conductivity – as diagnostic criteria.

Microwave technologies for treatment

Plasma medicine is one of the most modern synthetic scientific directions, born at the junction of plasma and Biomedicine physics, dealing with fundamental and applied issues of interaction between plasma and living matter. In this case, the greatest attention of researchers attracts the field of plasma medicine associated with the disclosure of biological and sanogenetic effects of cold plasma. Currently, the cold plasma is usually understood as ionized gas of different composition, cooled to a temperature comparable to the physiological (30-40 C). In recent decades for this factor a number of effects is potentially useful for medical purposes have been demonstrated experimentally and clinically. Among them, the most well studied and described antibacterial activity associated with the direct damaging effect of cold plasma on the cell wall of microorganisms. On the other hand, with a more thorough analysis of even this aspect of the problem, it reveals numerous poorly studied issues, including the effectiveness of the action, the absence of damage to the own tissues of the macroorganism, etc.

Special interest, in our opinion, have a bioregulatory properties of cold plasma in relation to functional and metabolic parameters of living systems. Thus, the pro-regenerative activity of the factor [6, 14], its ability to inhibit tumor growth [4, 10], etc. that was demonstrated earlier. Undoubtedly, the given empirical facts require multistage verification, but the very presence of such data testifies to the presence of secondary, indirect biological effects in cold plasma, which makes it possible to consider it as a potential bioregulator.

In our previous studies, is performing both in vitro and in vivo, the existence of secondary bioregulatory properties in cold plasma was shown and verified. In particular, even a short-term treatment (1-3 min.) of blood samples by the flow of helium cold plasma led to the formation of the biosystem response (by metabolic and physico-chemical criteria), and it is important to emphasize the dose dependence of the detected shifts [2, 3]. It should also be noted that the nature of the changes significantly differed from the "pattern" of the response to a similar effect of non-ionized helium flow from the same source [3]. Interestingly, the reaction of blood isolated from the body as a simple model biosystem as a whole was co-directed to shifts of the same blood parameters of rats exposed to short-term (1-2 min.) exposure to cold plasma on the pre-epilated areas of the back. As in the case of in vitro experiments, in this case shown moderate antioxidant activity of the factor, its positive effect on the intermediate link in the energy exchange etc. in addition, it was demonstrated modulating effect on the parameters of systemic and local hemodynamics.

Thus, plasma biomedicine is a promising, dynamically developing direction, integrating biophysical and biomedical approaches and capable of forming fundamentally new medical technologies, potentially useful for the correction of various diseases, pathological conditions, injuries and burns.

References

1. *Martusevich A.K., Peretyagin S.P., Vanin A.F.* The study of some porducts is generating with medical device for the synthesis of NO-containing cold plasma // Medical physics. 2012. No 4. P. 80-86.

2. *Martusevich A.K., Soloveva A.G., Yanin D.V., Galka A.G., Krasnova S.Yu.* The influence of gelium cold plasma on the parameters of blood oxidative metabolism in vitro // Gerald of New Medical Technologies. 2017. V. 24, No 3. P. 163-166.

3. *Martusevich A.K., Yanin D.V., Bogomolova E.B., Galka A.G., Klemenova I.A., Kostrov A.V.* Possibilities and perspectives of the use of microwave tomography in sin testing // Biomedical Radioelectronics. 2017. No 12. P. 3-12.

Terahertz quantum cascade lasers: what way forward?

Alessandro Tredicucci[1,2]

[1]Dipartimento di Fisica “E. Fermi", Università di Pisa, Largo Bruno Pontecorvo 3, Pisa 56127 (Italy)
[2]NEST, CNR Istituto Nanoscienze and Scuola Normale Superiore, piazza San Silvestro 12, 56127 Pisa (Italy)
alessandro.tredicucci@unipi.it

The first quantum cascade laser (QCL) was realized in the mid-infrared at Bell Laboratories in 1994 [1], bringing to life a concept that was developed already in the early seventies [2]. Even though from the very beginning it was argued that this device could be best operated in the THz (far-infrared) range of the electromagnetic spectrum, it was only in 2002 that the first working THz QCL was demonstrated [3]. Soon afterwards, the progress was very rapid; in the space of 2-3 years operating temperatures were raised to > 160 K, single-mode DFB devices were produced, applications as local oscillators in heterodyne transceivers were implemented, frequency coverage was extended to the whole 1-5 THz region. In the last few years, technological advancement has continued to improve performances, albeit at a much slower pace. The maximum operating temperature has now reached close to 200 K [4] (225 K in magnetic field [5]) and about 1 W peak output power has been demonstrated [6].

Several beam engineering techniques have also been implemented, with the scope of enhancing spectral purity, improving beam quality and achieving vertical emission [7]. In parallel, various approaches have been devised that allow frequency tunability of the emitted light [8], with the most efficient schemes achieving a tuning range of almost 10% of the central emission frequency.

For metrological applications, however, very high accuracy in the determination of the THz QCL frequency is needed, which can be obtained by phase-locking THz QCLs to ultra-stable microwave references, or directly to a free-space THz comb [9]. Furthermore, active mode locking of THz QCLs has been demonstrated by modulation of the drive current at the cavity round-trip frequency [10], and, more recently, even the generation of frequency combs directly from THz QCLs has been achieved by employing dispersion compensated waveguides and an intrinsic χ_3 non-linearity [11].

This talk will review the long road trodden by THz QCLs from their origins to the latest breakthroughs, and discuss present strengths and weaknesses in view of their use both for scientific purposes and widespread industrial applications.

In particular it will focus on the very relevant goal of combining low divergence regular beam profiles and single mode, vertical emission with a low device power consumption. This is a crucial requirement in order to keep cooling equipment (with the ensuing costs and encumbrance) to a minimum. In this direction, different approaches to miniaturization will be discussed, either making use of resonator designs mixing photonic and electronic concepts [12] or the exploitation of novel 2D materials.

Furthermore, it will examine new application ideas and configurations, ranging from microscopy with a self-detection scheme [13], to direct implementation in the field, for instance in monitoring water content of living plants [14].

References

1. *J. Faist, F. Capasso, D. L. Sivco, C. Sirtori, A. L. Hutchinson, and A. Y. Cho,* Quantum Cascade Laser // Science **264**, 553 (1994).
2. *R. Kazarinov and R. Suris,* Possibility of the amplification of electromagnetic waves in a semiconductor with a superlattice // Soviet Physics - Semiconductors **5**, 707 (1971).
3. *R. Köhler, A. Tredicucci, F. Beltram, H. E. Beere, E. H. Linfield, A. G. Davies, D. A. Ritchie, R. C. Iotti, and F. Rossi*, Terahertz semiconductor heterostructure laser // Nature **417**, 156 (2002).
4. *S. Fathololoumi, et al.,* Terahertz quantum cascade lasers operating up to ~200 K with optimized oscillator strength and improved injection tunneling // Opt. Express **20**, 3331 (2012).
5. *A. Wade, et al.,* Magnetic-field-assisted terahertz quantum cascade laser operating up to 225 K // Nature Photon. **3**, 41 (2009).
6. *L. Li, et al.,* Terahertz quantum cascade lasers with >1 W output powers // Electron. Lett. **50**, 309 (2014).
7. *L. Mahler and A. Tredicucci,* Photonic engineering of surface-emitting terahertz quantum cascade lasers // Laser & Photon. Rev. **5**, 647 (2011).
8. *M. S. Vitiello and A. Tredicucci*, Tunable Emission in THz Quantum Cascade Lasers // IEEE Trans. THz Sci. Techn. **1**, 76 (2011).
9. *L. Consolino, et al.,* Phase-locking to a free-space terahertz comb for metrological-grade terahertz lasers // Nature Comm. **3**, 1040 (2012).
10. *S. Barbieri et al.*, Coherent sampling of active mode-locked terahertz quantum cascade lasers and frequency synthesis // Nature Photon. **5**, 306 (2011).
11. *D. Burghoff et al.*, Terahertz laser frequency combs // Nature Photon. **8**, 462 (2014).
12. *L. Masini, et al.*, Continuous-wave laser operation of a dipole antenna terahertz microresonator // Light: Sci. & Appl. **6**, e17054 (2017).
13. *M. C. Giordano, et al.*, Phase-resolved terahertz self-detection near-field microscopy // Opt. Express **26**, 18423 (2018).
14. *L. Baldacci, et al.,* Non-invasive absolute measurement of leaf water content using terahertz quantum cascade lasers // Plant Methods **13**, 51 (2017).

Extreme THz fields from near and mid-infrared laser filaments

Stelios Tzortzakis

Science Program, Texas A&M University at Qatar, P.O. Box 23874, Doha, Qatar
Institute of Electronic Structure and Laser, FORTH, P.O. Box 1527, 71110, Heraklion, Greece
Department of Materials Science and Technology, University of Crete, P.O. Box 2208, 71003, Heraklion, Greece

The nonlinear propagation of ultrashort laser pulses in the form of solitons, filaments and light bullets is an exciting research field [1]. Beyond the basic studies on the complex spatio-temporal phenomena involved, the field is driven significantly by its numerous applications, like for example in materials engineering [2], remote spectroscopy [3], but also for their use as powerful secondary sources across the electromagnetic spectrum [4].

Here we discuss our recent advances in developing intense THz secondary sources using tailored laser filaments [5]. We also demonstrate that one may obtain powerful THz radiation using unconventional media, like liquids, where the medium presents strong linear absorption [6]. The mechanism responsible for this counterintuitive result is a phase locked second harmonic component in the filament that results in strong transient electron currents that radiate intense THz fields. Finally, we will also be discussing the way in achieving extreme THz electric and magnetic fields, in excess of GV/cm and kT strengths respectively, using intense two-color mid-infrared filaments [7].

[1] P. Panagiotopoulos, D. G. Papazoglou, A. Couairon, and S. Tzortzakis, "Sharply autofocused ring-Airy beams transforming into nonlinear intense light bullets," Nature Communications **4**, 2622 (2013)

[2] M. Chanal, V. Y. Fedorov, M. Chambonneau, R. Clady, S. Tzortzakis, and D. Grojo, "Crossing the threshold of ultrafast laser writing in bulk silicon," Nature Communications **8**, 773 (2017)

[3] S. Tzortzakis, D. Anglos, and D. Gray, "Ultraviolet laser filaments for remote laser-induced breakdown spectroscopy (LIBS) analysis: applications in cultural heritage monitoring," Opt. Lett. **31**, 1139-1141 (2006)

[4] Kang Liu, D. G. Papazoglou, A. D. Koulouklidis, S. Tzortzakis, X.-C. Zhang, "Enhanced terahertz radiation emission from abruptly autofocusing beams," Optica **3**, 605-608 (2016)

[5] A. D. Koulouklidis, D. G. Papazoglou, V. Y. Fedorov, and S. Tzortzakis, "Phase Memory Preserving Harmonics from Abruptly Autofocusing Beams," Phys. Rev. Lett. **119**, 223901 (2017)

[6] I. Dey, K. Jana, V. Y. Fedorov, A. D. Koulouklidis, A. Mondal, M. Shaikh, D. Sarkar, A. D. Lad, S. Tzortzakis, A. Couairon, and G. R. Kumar, "Highly efficient broadband terahertz generation from ultrashort laser filamentation in liquids," Nature Communications **8**, 1184 (2017)

[7] V. Fedorov and S. Tzortzakis, “Extreme THz fields from two-color filamentation of mid-infrared laser pulses,” arXiv:1708.07310 (2017), Phys. Rev. A **97**, 063842 (2018)

Measurement of radome material for 77/79 GHz automotive radar integration

Neidhardt, Steffen*; Heuel, Steffen; Koeppel, Tobias; Ahmed, Sherif
* steffen.neidhardt@rohde-schwarz.com, Rohde & Schwarz, Munich, Germany

***Abstract*—Automotive radars operate mainly in 77 GHz and 79 GHz frequency bands as 24 GHz radars are phasing out. These radars are integrated into bumpers of the car or mounted behind so called design emblems. These plastic materials need to be RF transparent to let the signals from the radar sensors pass without distortion. However, due to different paintings and coatings of bumpers low RF transparency and non-homogeneity can cause radars to malfunction and lower the radar performance. Testing the RF performance of materials requires typically a network analyzer and takes a long time. This paper presents a new measurement method to test and verify radome materials within seconds.**

***Index Terms*—automotive radar, 77/79 GHz, radome, bumper, integration**

I. INTRODUCTION

Advanced driver assistant systems (ADAS) in cars assist the driver and increase road safety. Key enabling technologies in this area, other than camera and Lidar sensors, are automotive radar sensors. These radars are covered by a masking known as a radome, which is constructed from a transparent RF material. Radomes can be an emblem or a car bumper with integrated radar units. Although an emblem may be underestimated as a simple plastic cover, it is actually a sophisticated element that often negatively impacts radar detection performance and accuracy. Emblems and car bumpers need to satisfy the requirements of optical appearance which is usually a conflicting requirement to the RF performance needed for 76 GHz to 81 GHz operation. This paper explains a novel radome measurement method and discusses the radomes influence on the accuracy of the angle of detection achieved with advanced radars.

II. RADOME INFLUENCES

The accuracy of a radar depends on many factors, such as hardware components, software processing and the radar echo signal itself. Parameters of signal echoes with lower signal to noise ratio (SNR) can be measured less accurately than signals with high SNR. In addition, effects such as multipath propagation and distortion due to radomes greatly impact measurement accuracy. Inaccuracies in the azimuth measurement cause the target to appear misplaced. An angular measurement error of only one degree at the radar sensor, for example, would cause a target in the 100 m range to appear to be misplaced by 1.75 m in azimuth, Fig. 1. It would be interpreted as being located in the neighboring lane. In practice, angular accuracy for such far distances must be significantly less than 1 for reliable operation. Inhomogeneous material distorts the wavefront, which results in less accurate angular measurements. The radar sensor calibration is no longer sufficient since the calibrated radar can be mounted behind any indeterminate radome from a different manufacturer.

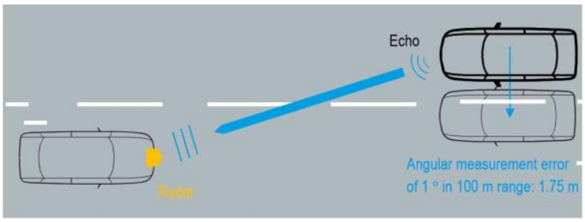

Fig. 1. Wrong azimuth angle measurement due to inhomogeneity of the radome.

For a modern radar sensor with an antenna array receiver frontend, the azimuth (and sometimes also the elevation angle) is estimated using phase and amplitude relations based on digital beamforming on the receive side. To get the best azimuth measurement accuracy, every radar sensor needs to be calibrated which is done in production without the radome or bumper part. The car manufacturer integrates this calibrated radar sensor into the car, often behind an emblem or the bumper. The radomes transmission loss increases the two-way attenuation of the radar signal, which influences the maximum detection range of the radar. The power level of a transmitted radar signal is reduced by the range R to the target and by R4 on the way back. For a 77 GHz radar system with 3 W output power, 25 dBi antenna gain, a target with 10 sqm radar cross-section and a minimum detectable signal of 90 dBm, the maximum range of this configuration would be 109.4 m according to the range equation. If the radome has 3 dB two-way attenuation, the maximum range of the same radar measuring the same target would decrease to 92.1 m. That is approximately 16% less range.

However, it is not only material attenuation that has a great impact. The material reflectivity and homogeneity also play an important role. Reflections and RF mismatch of the material cause direct signal reflections in close range to the radar. The signals are received and downconverted in the receiver chain, reducing the radars detection sensitivity. Many car manufacturers try to mitigate this effect by tilting the radomes (not only for design reasons) in order to reflect the transmitted radar somewhere other than directly back into the receiver frontend. This solution, of course, has plenty of mechanical limitations, not to mention the expected loss of RF energy due to these parasitic reflections.

For a modern radar sensor with an antenna array receiver frontend, the azimuth (and sometimes also the elevation angle) is estimated using phase and amplitude relations based on digital beamforming on the receive side. To get the best azimuth measurement accuracy, every radar sensor needs to be calibrated which is done in production without the radome or bumper part. The car manufacturer integrates this calibrated radar sensor into the car, often behind an emblem or the bumper. The radomes transmission loss increases the two-way attenuation of the radar signal, which influences the maximum detection range of the radar. The power level of a transmitted radar signal is reduced by the range R to the target and by R4 on the way back. For a 77 GHz radar system with 3 W output power, 25 dBi antenna gain, a target with 10 sqm radar cross-section and a minimum detectable signal of 90 dBm, the maximum range of this configuration would be 109.4 m according to the range equation. If the radome has 3 dB two-way attenuation, the maximum range of the same radar measuring the same target would decrease to 92.1 m. That is approximately 16% less range.

However, it is not only material attenuation that has a great impact. The material reflectivity and homogeneity also play an important role. Reflections and RF mismatch of the material cause direct signal reflections in close range to the radar. The signals are received and downconverted in the receiver chain, reducing the radars detection sensitivity. Many car manufacturers try to mitigate this effect by tilting the radomes (not only for design reasons) in order to reflect the transmitted radar somewhere other than directly back into the receiver frontend. This solution, of course, has plenty of mechanical limitations, not to mention the expected loss of RF energy due to these parasitic reflections.

III. TODAY'S MATERIAL CHARACTERIZATION PROCEDURE

Today there exist different measurement procedures for characterization of materials. Commonly a vector network analyzer (VNA) is calibrated at the connector calibration plane and the material under test (MUT) is placed in a measurement fixture / sample holder. A two-port network analyzer measures the S-parameters of the MUT (e.g. radome) mounted in the measurement fixture [1], Fig. 2. The incident, reflected and transmitted signals are processed by the network analyser and the S-parameters are converted by a selected conversion technique (e.g. NRW, NIST iterative, New noniterative, SCL) to the dielectric properties ǫr and µr. For example, the Nicholson-Ross-Weir (NRW) method provides a direct calculation of both the permittivity and permeability from the S-parameters. It is the most commonly used method for performing such conversion by using all four S-parameters of the material under test.

These methods provide permittivity and permeability parameters for the material, but do not resolve the measurements in azimuth and elevation. The parameters are valid for the area which the transmitting and receiving antenna cover. In case these parameters should be measured over the entire surface of the material, the antennas have to be moved precisely in azimuth (x-direction) and elevation (y-direction) dimensions and S-parameters have to be recorded per position. This measurement method takes several minutes. The advantage on the other hand are dielectric parameters which can also be used in simulation tools or further evaluation. However, these tests are not practical for quick overview or even production measurements.

Alternatively a radar can be mounted behind the material and the impact on the measurement results against reference targets can be measured Fig. 3. Therefore several corner reflectors are mounted in front of the radar and the positions are measured without the radome cover present. Comparing now the deviation of these positions without and with radome present one can draw conclusions on the impact of the material. However, this is rather a pass or fail test without having deeper knowledge of the material itself. Also this test is highly radar dependend and tests only the impact on certain azimuth / elevation angles while considering the radome to be homogeneous.

IV. NOVEL MEASUREMENT TECHNIQUE

Instead of testing transparent 77/79 GHz radar material with a golden device or a two-port network analyser, a proposed

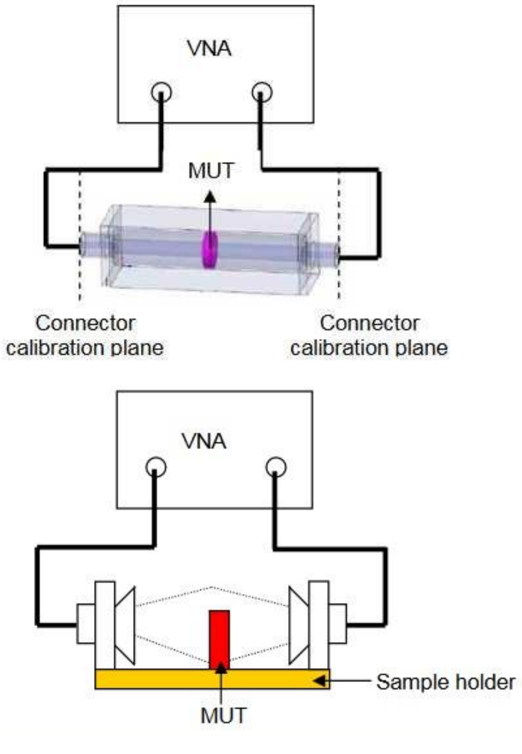

Fig. 2. Today's measurement technique using a VNA

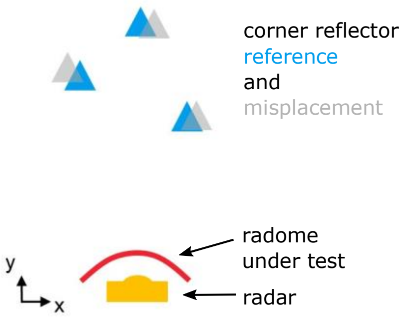

Fig. 3.Today’s measurement technique using a radar and referenc reflectors

novel measurement method combines a transmission measurement with three-dimensional, high-resolution radar imaging in the frequency band used later by the radar itself. This is done using the R&S QAR system (Fig. 4). A multi-antenna array consisting of several hundreds of transmit and receive antennas operating from 75 GHz to 82 GHz is used. This measurement system can measure the range, azimuth and elevation with millimeter resolution. It operates at the same frequency band as an automotive radar and therefore sees what an automotive radar would see (if it also had hundreds of transmit and receive antennas). Thanks to the large aperture, the resolution of the test system is much higher than automotive radars and it can visualize the measurement as an image.

The material under test (e.g. radome) is placed in front the test system, which performs a two-stage measurement. First, a reflectivity measurement determines the amount of energy that is being reflected by the radome material under test (MUT). This is the energy that does not pass through the radome and contributes to performance degradation. Reflected signals decrease the performance of the radar and can even interfere with the received signals. Areas with high reflectivity can have various causes, such as material defects, air gaps, undesired interaction between several layers of materials, excessive amount of certain materials or foreign objects. The measurement method achieves a spatially resolved reflectivity measurement result for a MUT by linking the information collected by the distributed, coherent transmit and receive antennas. The receive signals are gated and processed for all receive antennas, which results in a high-resolution 3D radar image. The resulting millimeterwave image enables intuitive as well as quantitative evaluation of the MUTs reflection behavior. For illustration purposes, we manufactured radome material where the R&S logo was milled with different thickness, as shown in Fig.5.

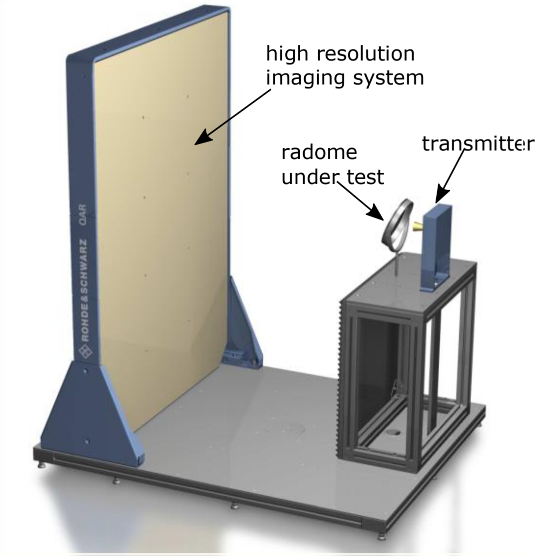

Fig. 4. Novel measurement technique using a multistatic array radar

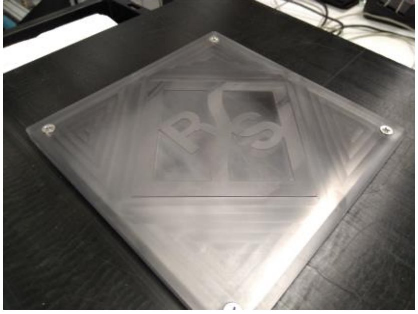

Fig. 5. Rohde & Schwarz embleme camera picture

A. Reflectivity Measurement

Compared to the network analyzer S-parameter measurement and calculation of dielectric properties, this method does a high resolution mm-wave picture from the material under test (basically the multistatc array it is also a network analyser, but just with 1500 RF ports, which measurement responses are treated differently). However, from the mmwave picture not the dielectric properties are calculated, but the mean reflectivity value per pixel and transmission loss of the material. These are different parameters, but result in the same conclusion - which is - decide if the material ”passed” or ”failed” the test to decide if it can be used with a radar or not. In addition a high resolution picture and transmission loss curve allow debugging.

The high-resolution radar image in Fig. 6 visualizes what an automotive radar sensor would perceive when covered by this radome if it would have super high resolution in azimuth and elevation (called pixel here). The color scale describes the reflectivity. The dark color indicates minimal reflectivity and brightness indicates high reflectivity. Metal, which cannot be penetrated by automotive radar signals, would appear white (e.g. screws in the four corners). It can be seen that the radome image indicates high reflectivity and inhomogeneity on the R&S logo. The increased thickness of 0.5 mm in the R&S logo area is therefore sufficient to cause major disturbances in radar performance on the street. In this example, calculating the features mean reflectivity and standard deviation in the middle area, where the radar sensor is usually mounted, yields:

Reflectivity measurement:
- mean reflectiviy: -11 dB
- standard deviation: -17.7 dB.

In many practical cases, this reflection is too high to maintain acceptable radar operation. In practice, the expected reflectivity depends on the sensitivity of the radar unit and the maximum detection distance to be covered.

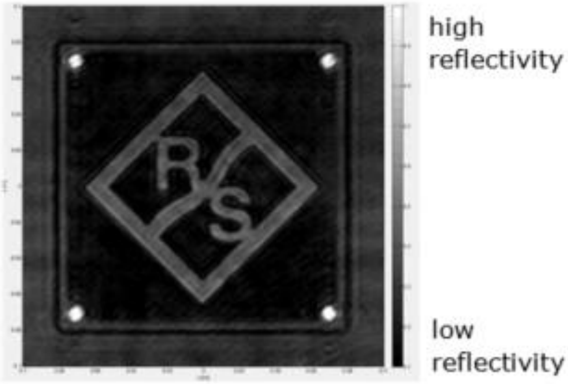

Fig. 6. Rohde & Schwarz embleme mm-wave picture

B. Transmission Measurement

In a second stage, the frequency matching and attenuation of the radome material is measured. A transmitter module is located behind the MUT on the MUT table. The transmitter uses a frequency sweep to cover a selected frequency span. This allows exact evaluation of the MUT's transmission frequency response. The frequency response delivers detailed information about the RF matching of the MUT at the exact frequency band intended for radar operation. It is therefore independent of the actual signal waveform utilized by the radar unit, which facilitates the testability and optimization of the radome itself. The measured one-way attenuation versus frequency of the radome is shown on the right side in Fig. 7. Since automotive radars operate in the 76 GHz to 81 GHz band, attenuation should be kept low across this band. Depending on the thickness of the material, its air gaps and RF matching, a good radome should maintain a low attenuation at the desired frequencies.

Transmission measurement:
- attenuation 76-77 GHz: 0.8 dB
- attenuation 79-81 GHz: 0.6 dB.

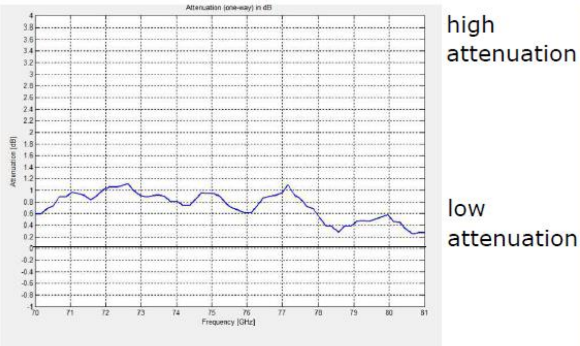

Fig. 7. Rohde & Schwarz embleme transmission measurement

A more sophisticated example for commercial radomes with a 3D design typically results in a transmission measurement as shown in Fig. 8. Drawn from the transmission measurement this radome would have various performance issues:

- like the frequency matching is incorrectly placed around 71 GHz instead of 76 GHz often caused by increased thickness of some radome layers.
- significant increase in the standing wave ratio within the 79 GHz band, which identifies high reflections at the radome boundaries and therefore a strong interference phenomenon
- overall one-way attenuation is high, which results in a significant reduction in the detection range.

V. SUMMARY

Radars are common in all newer series cars. Integration behind bumpers and emblems makes them also attractive for car designers. Without high-quality radomes, objects with low radar cross-sections, such as pedestrians, would most likely go undetected and may even appear under a false azimuth angle. Even larger objects at far distances could be wrongly identified and measured at a different position when the radar signal becomes too distorted due to inhomogeneous material. This paper presented a novel measurement method that can be applied for any kind of automotive radomes, such as the ones used in emblems, bumpers or front grills that cover automotive radar sensors operating in the 75 GHz to 82 GHz band. Based on a massive multistatic

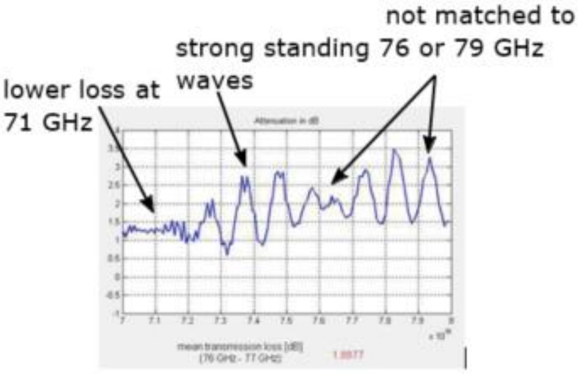

Fig. 8. Commercial embleme transmission measurement

array technique, this method measures and calculates the mean reflectivity and standard deviation of a defined area (homogeneity) and the transmission loss over the complete frequency range within a few seconds.

REFERENCES

[1] Kuek Chee Yaw, Rohde & Schwarz Application Note, ”Measurement of Dielectric Material Properties”, RAC 0606-0019 1 4E, April 2012